Journal of Energy Chemistry 56 (2021) 162–170

Contents lists available at ScienceDirect

Journal of Energy Chemistry

journal homepage: www.elsevier.com/locate/jechem

http://www.journals.elsevier.com/journal-of-energy-chemistry/

Diverse morphologies of zinc oxide nanoparticles and their electrocatalytic performance in hydrogen production

Veronica M. Sofianos [a,b,*], Junqiao Lee [c], Debbie S. Silvester [c], Pralok K. Samanta [b], Mark Paskevicius [a], Niall J. English [b], Craig E. Buckley [a]

[a] Department of Physics and Astronomy, Fuels and Energy Technology Institute, Curtin University, Perth, Bentley 6102, Australia
[b] University College Dublin, School of Chemical and Bioprocess Engineering, Belfield, Dublin 4, Ireland
[c] Curtin Institute for Functional Molecules and Interfaces, School of Molecular and Life Sciences, Curtin University, Perth, Bentley 6102, Australia

ARTICLE INFO

Article history:
Received 5 April 2020
Revised 23 July 2020
Accepted 26 July 2020
Available online 2 August 2020

Keywords:
ZnO nanoparticles
Nanocatalysts
Electrocatalysis
Hydrogen production
Water splitting

ABSTRACT

Hydrogen is considered an attractive alternative to fossil fuels, but only a small amount of it is produced from renewable energy, making it not such a clean energy carrier after all. Producing hydrogen through water electrolysis is promising, but using a cost-effective and high-performing catalyst that has long-term stability is still a challenge. This study exploits, for the first time, the potential of zinc oxide nanoparticles with diverse morphologies as catalysts for the electrocatalytic production of hydrogen from water. The morphology of the nanoparticles (wires, cuboids, spheres) was easily regulated by changing the concentration of sodium hydroxide, used as the shape controlling agent, during the synthesis. The spherical morphology exhibited the highest electrocatalytic activity at the lowest potential voltage. These spherical nanoparticles had the highest number of oxygen vacancies and lowest particle size compared to the other two morphologies, features directly linked to high catalytic activity. However, the nanowires were much more stable with repeated scans. Density-functional theory showed that the presence of oxygen vacancies in all three morphologies led to diminished band gaps, which is of catalytic interest.

1. Introduction

Hydrogen is considered as an attractive energy vector due to its high energy to mass ratio (120 MJ/kg) that can easily replace fossil fuel consumption meeting global energy demands. When produced from renewable energy, it is considered as "green" hydrogen. To date, the most advanced method to produce green hydrogen is through water electrolysis. This can only be achieved with the use of a catalyst on the cathode for the hydrogen evolution reaction (HER) to take place [1]. However, the majority of catalysts used so far are platinum based alloys, which, even though show high performance and long-term durability, are high in cost and their materials are scarce [2–4]. As a consequence, large-scale production of green hydrogen through water electrolysis is not economically viable. Hence, hydrogen is predominately produced through steam-reforming of fossil fuels such as methane [5]. A catalyst that is cost-effective, both in terms of the raw materials and synthesis method, and has high catalytic efficiency and long-term stability is vital for the establishment of the green hydrogen production. For this purpose, the potential of zinc oxide nanoparticles to be used as catalysts for the HER is exploited.

Zinc oxide (ZnO) is a semiconductor material with a direct bandgap of 3.37 eV that has a vast variety of applications ranging from electronics to cosmetics [6–11]. It is commonly used in solar cells, photo detectors, light emitting diodes, ultraviolet lasers, chemical gas sensors, photo- and electrocatalysis, sunscreens, paints, and in the food industry [12–21]. One reason for ZnO being such an attractive and versatile material is due to the fact that its physical and chemical properties are directly linked to its morphology and particle size [22–25]. The relationship of properties and possible applications to morphology is clearly evident on the nano-scale. Therefore, it is important to be able to control the morphology of ZnO nanoparticles during synthesis to achieve high-performing products.

Various synthetic techniques have been used over the years to produce ZnO nanoparticles, including chemical vapor deposition

* Corresponding author at: School of Chemical and Bioprocess Engineering, University College Dublin, Belfield, Dublin 4, Ireland.
E-mail address: mvsofianou@gmail.com (V.M. Sofianos).

https://doi.org/10.1016/j.jechem.2020.07.051

(CVD), pulsed laser deposition (PLD), hydrothermal and sol–gel methods, electrochemical deposition, microwave-assisted techniques and precipitation [26–37]. A shape controlling agent is most commonly used during synthesis to obtain ZnO nanoparticles with various morphologies and sizes. Citric acid and other citrates are often used during the hydrothermal method to produce hierarchical flower-like ZnO structures [38–40], whereas trisodium citrate has also been added in hydrothermal condition at various concentrations for the synthesis of hexagonal disks, porous and solid spheres [38]. Dimethylamine is another shape-controlling agent used in the sol–gel method for obtaining ZnO nanorods [41].

Although many efforts have been made to obtain ZnO nanoparticles with various morphologies and sizes, the majority of synthesis methods either use expensive shape controlling agents, relatively high temperatures (~200 °C), expensive equipment, or methods that involve multiple steps which are time consuming and labour intensive [42–44]. Herein, we report a simple one-step synthesis method for controlling the morphology of ZnO nanoparticles using a room temperature sol–gel method. Zinc acetate was used as the Zn precursor and sodium hydroxide as the shape controlling agent. By altering the pH levels of the zinc acetate solution from 8 to 10, and then to 12, by increasing the amount of sodium hydroxide added in the final solution, ZnO nanowires, nanocuboids and nanospheres were produced. Compared with other sol–gel methods, this approach is not only cost-effective, simple, and easily reproduced, but also can be used to effectively control the morphology to create well-defined ZnO nanoparticles that are uniform in size. Their structural, morphological and chemical properties were thoroughly investigated by X-ray diffraction (XRD), small angle X-ray scattering (SAXS), scanning electron microscopy (SEM), transmission electron microscopy (TEM), and X-ray photoelectron spectroscopy (XPS). To the best of our knowledge, this is the first study to report the influence of the ZnO morphology, particle size and oxygen vacancies on its electrocatalytic activity for hydrogen production *via* electrochemical water splitting.

2. Experimental

2.1. Synthesis of ZnO nanoparticles

ZnO nanoparticles with diverse morphologies were prepared using a sol–gel method. Specifically, three solutions were prepared by dissolving 20 mmol of zinc acetate ($Zn(CH_3CO_2)_2$, 99.99%, Sigma Aldrich) in 50 mL of absolute ethanol (≥99.8%, Sigma Aldrich) under vigorous stirring at room temperature. Sodium hydroxide (NaOH, 99.99%, Sigma Aldrich) was added to the above solutions in three different concentrations, as to achieve pH levels of 8, 10 and 12. The obtained solutions were vigorously stirred for 24 h to obtain a homogenous aged gel. The collected powder products were washed twice with distilled water and finally with absolute ethanol and dried in a furnace at 70 °C overnight. All three as-prepared samples were calcined in static air in a muffle furnace for 90 min at 600 °C after heating at 5 °C/min and then cooled to room temperature naturally.

2.2. Characterization techniques

Powder X-ray diffraction (XRD) was used for phase analysis using a D8 Advance (40 kV, 40 mA) diffractometer from Bruker, Germany with Cu-K_α radiation (8.04 keV). The measured 2θ range (20°–80°) was scanned using a 0.03° step size at 1.6 s/step, a sample rotational speed of 30 rpm and a 0.3° divergence slit in flat plate geometry. Morphological observations were carried out with a Zeiss Neon 40EsB (Zeiss, Germany) scanning electron microscope (SEM) and a FEI Talos FS200X G2 FEG transmission electron microspore (TEM). SEM specimens were prepared by placing a small amount of powder onto carbon tape and then coating them with a 3 nm layer of platinum to produce a conductive layer and reduce charging during SEM imaging. The TEM specimens were prepared by direct deposition of the powder samples onto a carbon coated Cu TEM grid. Chemical analysis of the ZnO nanoparticles was undertaken with a Kratos AXIS Ultra DLD X-ray photoelectron spectrometer in ultra-high vacuum equipped with an Al-K_α X-ray source (1486.7 eV). The data was analysed using the Casa XPS software, and calibrated using the surface adventitious C 1s peak at 284.5 eV and O 1s peak at 530.2 eV, respectively.

The particle size distribution and specific surface area were investigated by Small-Angle X-ray Scattering (SAXS) with measurements conducted at the Australian Synchrotron. The energy applied was 12 keV that corresponds to λ = 1.0333 Å, the camera length was 3343 mm and q range was from 0.005 to 0.246 $Å^{-1}$. The particle size distribution was modelled by the maximum entropy model as supplied in the Irena package [45–47]. The dimensions of the nanowire cross section were modelled by using the cylinder particle shape model, whereas for the nanocuboids and nanospheres dimensions the spheroid particle shape model was applied. The q range, for which the models were fitted accurately, was between 0.007 and 0.1 Å, and the values provided were trustworthy.

The measured intensities were normalised with the ScatterBrain software by use of a glassy carbon standard, scaled by the specimen thickness [48], and an empty sample holder covered by kapton tape subtracted as background. All three scattering patterns were modelled using the unified model [49] in Irena [50] and the power law index [48,50] for each pattern was determined. The power law index for the measured q range gives information regarding the size and shape of the scattering particles. The specific surface area, $S(r)$, was calculated following the approach of Beaucage (1), with the size of the probe used (r) equal to 4 Å, equivalent to the diameter of the nitrogen molecule, so that results were comparable with the specific surface areas measured using the BET method [51,52].

$$S(r) = Sr^{2-D}, \tag{1}$$

where D is the surface fractal dimension, and S (m^D/g) is given as (2),

$$S = \frac{2\pi\varphi(1-\varphi)B_s}{Q\rho_{\text{sample}}F(D)} \tag{2}$$

where, ρ_{sample} is the effective particle density and is equivalent to the particle mass divided by the particle volume, including the pore volume ($\rho_{\text{sample}} = \rho_{\text{base}}\frac{V_{\text{base}}}{V_{\text{bulk}}} = \rho_{\text{base}}\frac{d_{\text{sp}}^3}{d_{\text{tot}}^3}$, where ρ_{base} is the density of ZnO (5.1 g/cm^3), d_{tot} is the thickness of the known sample holder, d_{sp} is the sample thickness not including any porosity and was calculated from the X-ray transmission measurements), B_s is the surface fractal power law prefactor, Q (cm^{-1} $Å^{-3}$) is the high-q invariant (3), and $F(D) = \{\Gamma(5-D)\sin[(3-D)\pi/2]\}/(3-D)$, where Γ is the gamma function, $\varphi = \rho_{sample}/\rho_{base}$, ρ_{base} is the primary particle density.

$$Q = \int_0^\infty I(q)q^2dq = \frac{2\pi^2G_s}{V_{\text{base}}}, \tag{3}$$

where G_s (cm^{-1}) is the Guinier prefactor for the primary particle substructure and V_{base} is the volume of the primary particles and $I(q)$ is the absolute intensity.

2.3. Density-Functional Theory calculations

All of the Density-Functional Theory calculations were performed using plane-wave basis with plane-wave energy cutoff of 500 eV and general gradient approximation (GGA) for exchange–correlation energy functional in the version of Perdew, Burke and Ernzerhof (PBE) [53], as implemented in the Vienna Ab-initio Simulation Package (VASP 5.3.5) [54–57]. The unit cell of wurtzite ZnO (w-ZnO) consisted of 2 Zn and 2 O atoms. The w-ZnO 0001 surface was modeled using $3 \times 3 \times 2$ supercell, which contains 36 Zn and 35 O atoms. The Monkhorst-Pack method, with the gamma-centred k-point grid of $6 \times 6 \times 4$ and $4 \times 4 \times 1$, was adopted for integration in the Brillouin zone for bulk w-ZnO and $3 \times 3 \times 2$ supercell with O vacancy calculations. The DFT (PBE) + U methodology (with an additional Hubbard-like term, U) was used to consider strong on-site Coulomb interaction of localised electrons, which is not correctly described by PBE functional. The U value for 3d orbitals of Zn and 2p orbitals of O were considered as 10 and 7 eV [58]. Geometry optimisations were done before single-point energy calculations. The convergence criterion for the maximal force on atoms was 0.02 eV/Å with the self-consistent convergence accuracy was set at 10^{-6} eV. Our calculated band gap using PBE + U for bulk w-ZnO was 3.28 eV, which is close to the experimental value of 3.4 eV for bulk w-ZnO.

2.4. Evaluation of ZnO hydrogen evolution reaction electrocatalytic performance

2.4.1. Electrode preparation

5 mg of the ZnO nanoparticles of selected morphologies (nanowires, nanocuboids, and nanospheres) were loaded as catalysts into 3 mg of carbon black (Super P®Conductive 99+%, Alfa Aesar) and 50 μL of 5% Nafion® 117 solution (Sigma-Aldrich) to form the "ink". For the control, 5 mg of carbon black powder was added in place of the ZnO nanoparticles. Before drop-casting, the macrodisk glassy carbon (GC) electrode (CHI104, 3 mm diameter, CH Instruments Inc.) was cleaned using ethanol, and then polished with soft lapping pads (Buehler) and a diamond suspension (1 μm, Kemet), followed by alumina powder (0.05 μm, Kemet). The polished electrode was sonicated first in ethanol and then in ultrapure water for 5 min. Finally, it was rinsed using ethanol before blowing dried under a stream of dry air. The drop-casting solution was prepared by dissolving the as-prepared ink in 450 μL of absolute ethanol, and then sonicated for >1 h. 3 μL of the solution was carefully drop-casted on the macrodisk GC electrode, to produce a 4.2 g/m^2 electrode catalyst mass loading for each of the three ZnO morphologies before allowing to dry for >15 min.

2.4.2. Hydrogen evolution reaction setup and procedures

The hydrogen evolution reaction (HER) measurements were carried out in a borate buffered 0.5 M Na_2SO_4(aq) (≥99.5%, anhydrous, Powder/Certified ACS, Fisher Scientific) solution, prepared in ultrapure water (with a resistivity of 18.5 MΩ cm). The solution pH was carefully adjusted to 7.0, by using boric acid and di-sodium tetraborate (99.8% H_3BO_3 and 99.5% $Na_2B_4O_7$ respectively, AnalaR®, Bio-Strategy Limited). The buffer and pH level were carefully chosen to ensure that the ZnO nanoparticles were stable throughout the electrochemical experiments. ZnO nanorods were found by Liu et al. to be stable in a borate buffered solution even at higher pH levels between 9.5 and 12, exhibiting only minor morphological changes after their photoelectrochemical studies [59]. A 5 mL aliquot of the as-prepared buffered aqueous solution was then added into a glass beaker, and purged with nitrogen gas (>99.999%, Coregas) by bubbling (at a flow rate of 100 ccm) under intense stirring (2000 rpm) for more than 15 min. The stirring rate was then reduced to 1500 rpm, and the nitrogen line was lifted above the solution to maintain a nitrogenated environment within the cell. The modified GC electrode was then lowered into the solution to commence the HER measurements. All measurements were obtained *vs.* a Ag|AgCl|3 M KCl(aq) reference electrode (MF-2052, BASi). A graphite rod (MW-4131, BASi) was used as the counter electrode. To limit the built up of hydrogen bubbles, the HER measurements were conducted with a fast constant stirring rate of 1500 rpm. The position of the electrodes was fixed across all measurements to ensure consistency. Linear sweep voltammetry (LSV) was carried out at a scan rate of 5 mV/s, starting at the open circuit potential (OCP, ca. −0.15 V) and scanning in the negative direction, with the cut-off current set at −850 μA, using a μ-Autolab Type III potentiostat (Eco-Chemie) controlled by a NOVA 1.11.2 software. The currents, *I*, measured were divided by the surface area of the GC electrode (surface area of 2.83×10^{-5} m^2) to obtain the current densities, *J* (which corresponds to −30 A m^{-2} at −850 μA).

3. Results and discussion

3.1. Phase observations

The X-ray diffraction patterns of the three ZnO morphologies are presented in Fig. 1. Only one crystalline phase is present in all three diffraction patterns, ZnO (JCPDS 01-089-1397) with a wurtzite crystal structure (C_{6v}^4-P6$_3$mc) [60]. No other impurities of the remaining precursors were detected in the samples, indicating that zinc acetate completely reacted to form ZnO during the sol–gel synthesis method. The sharp peak intensities indicate that the nanoparticles are crystalline in nature [61, 62].

3.2. Morphological observations

SEM micrographs of the ZnO nanoparticles are presented in Fig. 2, and it can be seen that their morphologies are significantly different. ZnO nanowires (Fig. 2a) were obtained when the pH level of the solution during synthesis was adjusted to 8. When the pH level was increased to 10, and then 12, with the concentration of the Zn precursor remaining the same, the morphology altered from wires to cuboids, and then to spheres, respectively. It is noticeable that the increase in pH not only altered the morphology of the nanoparticles but also significantly decreased their particle sizes (Fig. 2b, c). To obtain micrographs with better resolution that would assist with the precise morphological analysis of the cuboids and spheres, TEM imaging of the samples was performed.

The change in morphology caused by the increase in pH during the synthesis indicates that the concentration of OH^- is the main

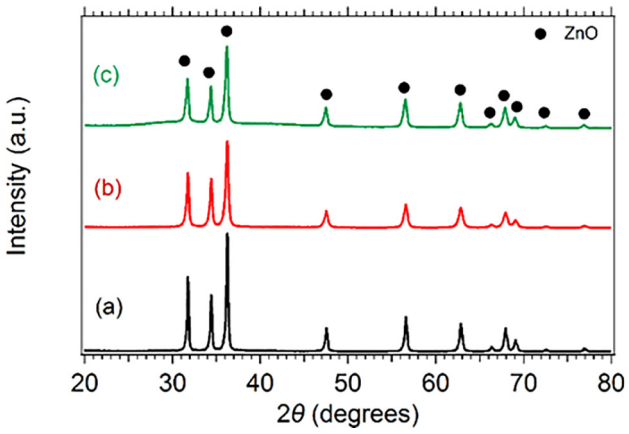

Fig. 1. XRD patterns of the ZnO (a) nanowires (pH = 8), (b) nanocuboids (pH = 10) and (c) nanospheres (pH = 12).

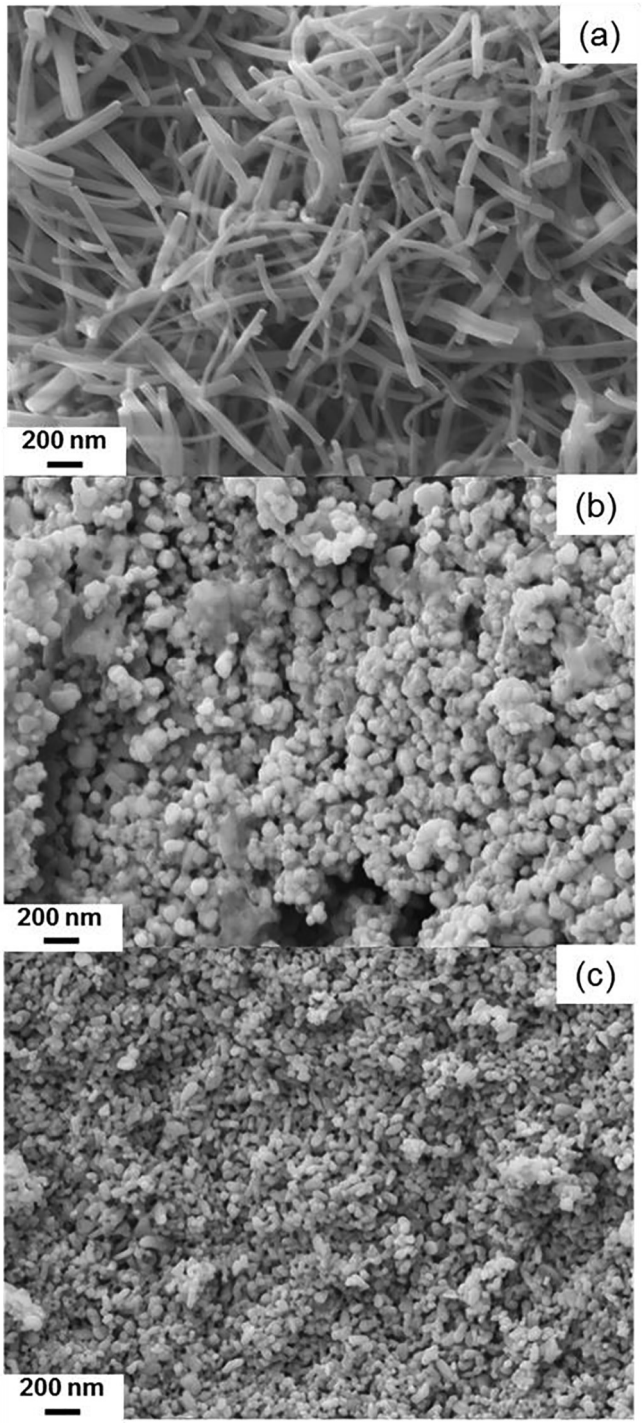

Fig. 2. SEM micrographs of (a) the ZnO nanowires (pH = 8), (b) nanocuboids (pH = 10) and (c) nanospheres (pH = 12).

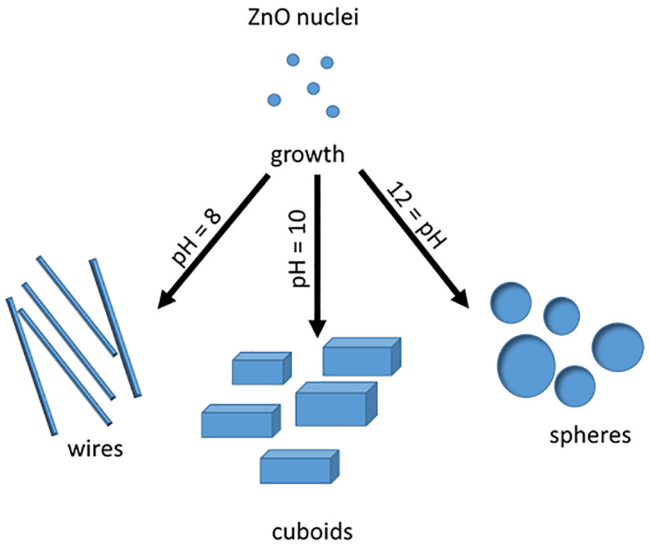

Fig. 3. Illustration of the proposed growth mechanisms of the as-prepared ZnO nanoparticles by changing the concentration of OH^- in the solution.

factor influencing particle growth [63,64]. The higher the concentration of OH^- ions, the more growth units are available in the solution. Therefore, at low pH levels (pH = 8) all the nuclei of ZnO will preferentially grow along the crystal habit (c-axis) to form wires (~900 nm in length as observed from the SEM image Fig. 2a). As pH increases, the concentration of OH^- ions increases in the solution, and the growth of the crystal in different directions other than the c-axis becomes more likely. Hence, at pH = 10 and 12 we obtain nanocuboids and nanospheres, respectively. Fig. 3 illustrates the proposed growth diagram of the as-prepared ZnO nanoparticles.

TEM micrographs of the ZnO nanocuboids and nanospheres are presented in Figs. 4 and 5 respectively. It can be seen that the nanocuboids have various sizes 40–90 nm, and the surface is smooth, since no significant colour contrast is observed in the micrographs indicating that the electron densities of the image plane is uniform. The electron diffraction pattern (inset in Fig. 4b) of the single nanocuboid in Fig. 4(b) shows that the nanocuboids are single crystals. As the concentration of OH^- increases, the ZnO nanoparticles change from cuboids to spheres. The size of the spheres is quite uniform, ranging between 50 and 60 nm, but they are not monodisperse (Fig. 5a). In Fig. 5(b) it is noticeable that the surface of the nanosphere is quite disordered with areas of dark and light grey throughout. This implies that the electron densities in the nanoparticle's image plane are uneven. This can be caused by oxygen vacancies in the ZnO's crystal lattice creating either a disordered crystal or a polycrystalline nanoparticle which is confirmed from the electron diffraction pattern (inset in Fig. 5b). The respective pattern no longer consists of single spots as it did for the nanocuboids (inset in Fig. 4b), indicating asymmetry in the crystal orientations or the presence of a polycrystalline particle. The polydispersity of the nanocuboids and nanoshperes, as well as their average particle size, is in agreement with the data collected using small angle X-ray scattering (Figs. 1S and 2S, Table 1), as discussed next.

3.3. Specific surface area calculations and particle size distribution

The specific surface area was calculated from SAXS data according to the Beaucage method [49], as previously described in section 2.2. The unified fit to the SAXS data for all three morphologies of ZnO allows us to determine the parameters necessary for the calculation of the specific surface area (see Table 1). X-ray transmission measurements (τ_s = 0.08, 0.51, and 0.13 for wires, cuboids and spheres respectively) during SAXS provide a measure of the bulk density of the samples containing the ZnO nanoparticles (4.7×10^{-5}, 8.8×10^{-7}, 2.5×10^{-8} g/cm^3 for wires, cuboids and spheres respectively) and the effective thickness of the sample (0.0042, 0.0011, 0.0003 cm for wires, cuboids and spheres respectively), φ, was equal to 9.1×10^{-6}, 1.7×10^{-7}, 4.8×10^{-9} for wires, cuboids and spheres, respectively. The total sample thickness (in-

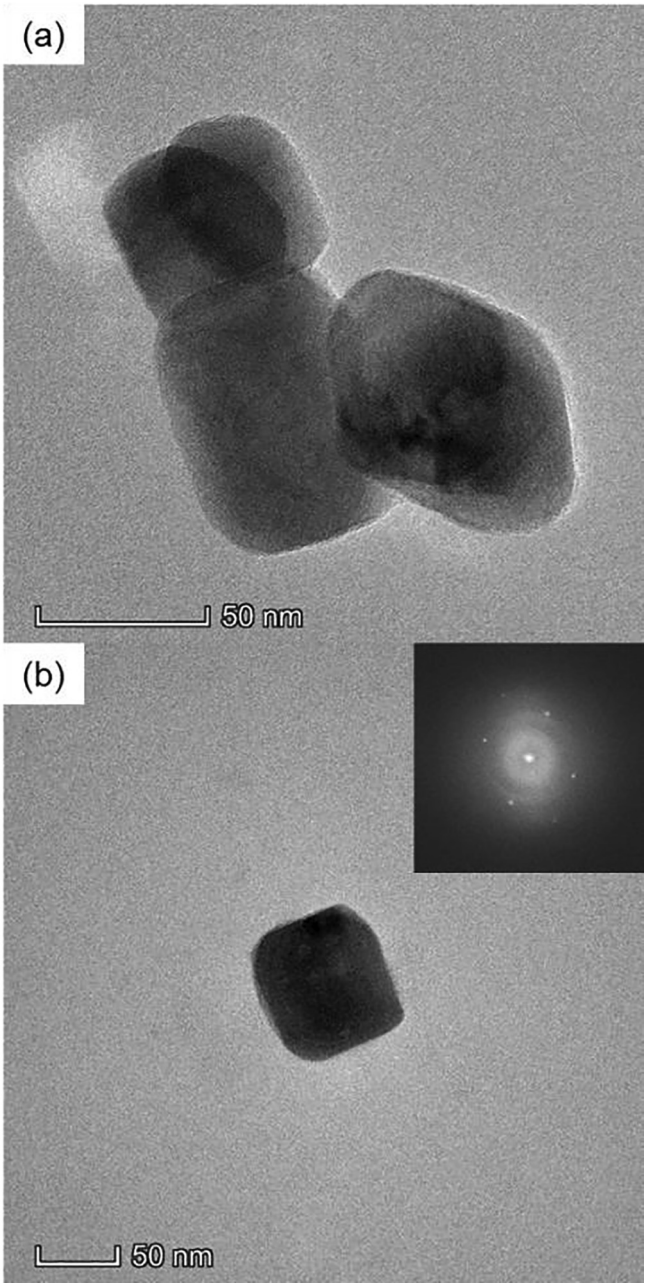

Fig. 4. TEM micrographs of the (a, b) ZnO nanocuboids (pH = 10) and the inset shows the electron diffraction pattern.

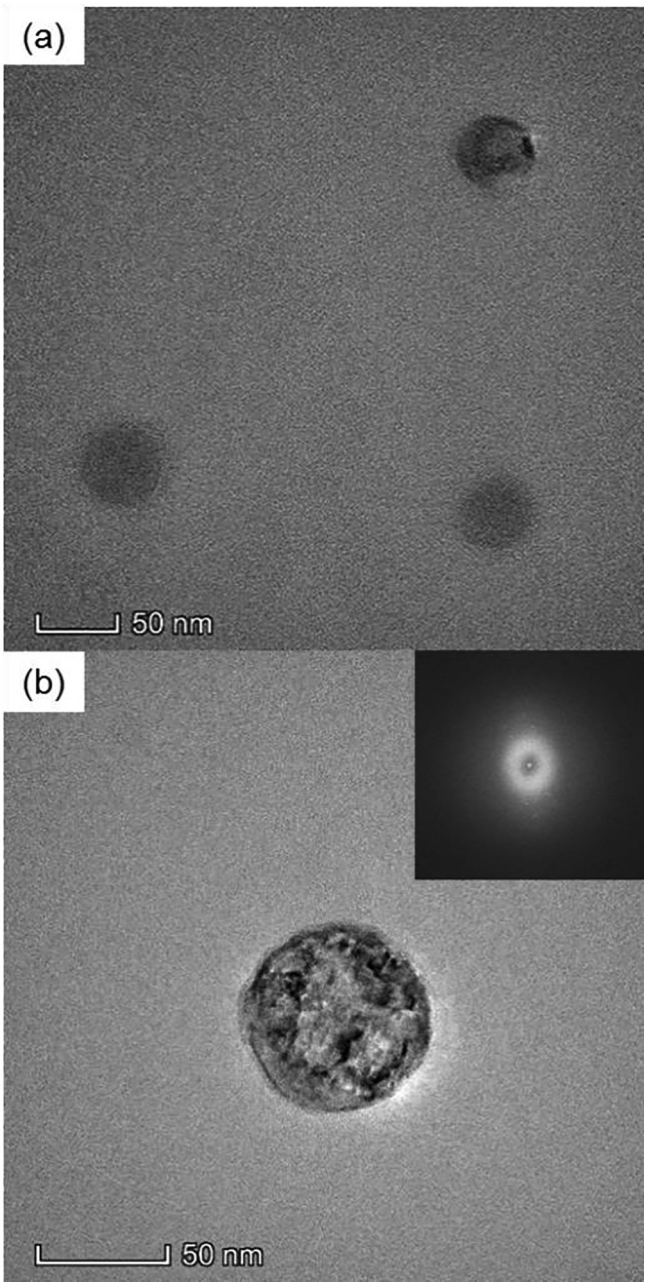

Fig. 5. TEM micrographs of the (a, b) ZnO nanospheres (pH = 12) and the inset shows the electron diffraction pattern.

cluding pore volume) was 0.1 cm, which was the actual thickness of the sample holder that contained the ZnO powder. The reason why the φ is so small is due to the fact that the sample holder had to contain the minimum amount of ZnO powder to avoid oversaturation of the detector. The calculated specific surface areas (*S*), together with the average particles size (*A.P.S*) are presented in Table 1. The values of *S* for all three morphologies are similar.

The nanocuboids exhibited the highest specific surface area of 36.1 ± 1.8 m^2/g, whereas for the nanowires it was 35.6 ± 1.8 m^2/g and for the nanospheres it was 30.4 ± 1.5 m^2/g. The average size for the nanocuboids was 89 ± 5 nm (Fig. 7b), the nanospheres was 51 ± 3 nm (Fig. 8b) and the average cross section of the nanowires was 79 ± 4 nm (Fig. 6b). The size distribution of the ZnO nanowires and nanocuboids showed a peak at about 6 nm that can be attrib-

Table 1
Parameters obtained for the calculation of the specific surface area (*S*) by modelling the SAXS patterns using a unified fit. The values of the specific surface areas as well as the average particle size (A.P.S.) are also presented.

ZnO sample	*D*	*Bs* ($cm^{-1}Å^{6-D}$)	*Q* (cm^{-1} $Å^{-3}$)	*F (D)*	*S* (m^2 g^{-1})	A.P.S (nm)
nanowires	2.146	0.000156	0.02203	2.0017	35.6 ± 1.8	79 ± 4 and 5 ± 1
nanocuboids	2.118	0.000035	0.00515	2.0044	36.1 ± 1.8	89 ± 5 and 7 ± 1
nanospheres	2.116	0.000154	0.02653	2.0045	30.4 ± 1.5	51 ± 3

uted to the presence of some smaller nanoparticles in their early stage of growth. All SAXS patterns showed two diffraction peaks at high q values (0.161 and 0.191 $Å^{-1}$). These diffraction peaks are more evident in the scattering pattern for the nanowires (Fig. 1S) and become less intense for the nanocuboids (Fig. 2S) and nanospheres (Fig. 3S), and are due to the high scattering nature of the samples. Specifically, when the intensity at the edge of the beamstop is high enough, then diffraction off the edge of the beamstop can occur, which will show in the scattering pattern of the measured sample.

3.4. XPS analysis

XPS measurements were carried out to investigate the presence of oxygen vacancies in the ZnO nanoparticles, which are directly linked to enhanced catalytic activity [65,66]. These vacancies are created by a combination of factors, such as the concentration of OH^- radicals present during the growth of the ZnO nanoparticles and the environment in which the nanoparticles were calcined [67]. Studies have shown that the concentration of OH^- present during the wet chemical synthesis of ZnO can create an increased number of surface defects with increased concentration, whereas calcining the nanoparticles in an oxygen environment, such as air, decreases the formation of oxygen vacancies [68]. In the present study, the concentration of OH^- was varied during the synthesis method, and the calcination environment was kept constant for all three samples. Therefore, the created oxygen vacancies in the ZnO nanoparticles are only related to the concentration of OH^- during synthesis.

The O_{1s} spectra was deconvoluted and fitted to three specific peaks [67], the Zn-O bond in the ZnO matrix (O_{lat}) at ~530 eV, oxygen vacancies (O_{vac}) at ~532 eV and oxygen that is chemically adsorbed (O_{ads}) at ~534 eV as shown in Fig. 6. Changes in the relative intensity of the O_{vac} peak are connected with the concentration of oxygen vacancies. It can be seen from Fig. 7 that as the concentration of pH increases so do both the atomic ratio of Zn to O, and the relative intensity of O_{vac}, indicating that a Zn rich surface is created with increase in pH, with the nanospheres having the highest number of oxygen vacancies on their surface. All three samples exhibit a high O_{lat} and low O_{ads} intensity, indicating strong Zn–O bonding and low concentrations of chemically adsorbed oxygen, respectively. The low concentration of chemically adsorbed oxygen in all three samples is due to their calcination in air at 600 °C for 4 h. The XPS survey spectra of the three ZnO morphologies are presented in Fig. 4S, together with the calculated atomic percentages of all elements present in the samples (Table 1S).

3.5. Electronic-structure calculation

Ab-initio Density-Functional Theory (DFT) was deployed to show that the presence of the oxygen vacancies on the (0001) surface of wurtzite ZnO (w-ZnO) decreased the band gap. The unit cell of w-ZnO, and a top view of a 3 × 3 × 2 w-ZnO super-cell with O vacancies on (0001) surface, are shown in Fig. 8(a and b), respectively. The partial charge on Zn atoms in bulk w-ZnO is +1.18 |e|. The partial charge on Zn atoms near the O-vacancy sites is around +1.18 ± 0.04 |e|. Thus, there is no change in partial charge on the atoms upon the introduction of a vacancy. However, in contrast, there is a major change in band gap upon vacancy formation (Fig. 8c). Bulk w-ZnO has a band gap of 3.28 eV, whereas the 3 × 3 × 2 w-ZnO super-cell with oxygen vacancies on its (0001) surface has a markedly diminished band gap of 2.25 eV. Thus, from a band-gap perspective, w-ZnO featuring an oxygen vacancy appears to be substantially more useful in the present electrocatalytic circumstances. Indeed, these findings reflect more broadly our DFT simulations finding that increasing oxygen vacancies concentrations tend to reduce band gaps.

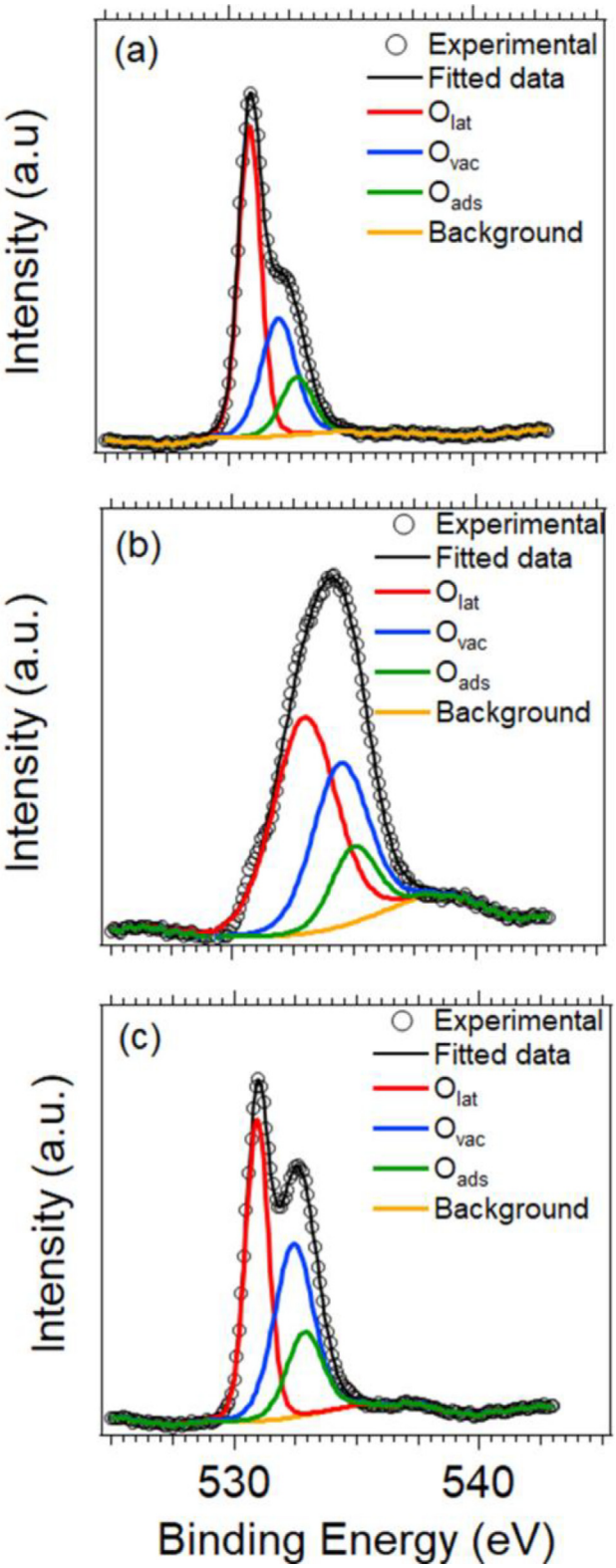

Fig. 6. O1s XPS spectra for the (a) nanowires (pH = 8), (b) nanocuboids (pH = 10) and (c) nanospheres (pH = 12). The spectrum is deconvoluted to three specific peaks: the Zn – O bond in the ZnO matrix (OLat) centred at ~ 530 eV, the oxygen vacancies (OVac) centred at ~ 532 eV and the oxygen chemically adsorbed (OAds) centred at ~ 534 eV.

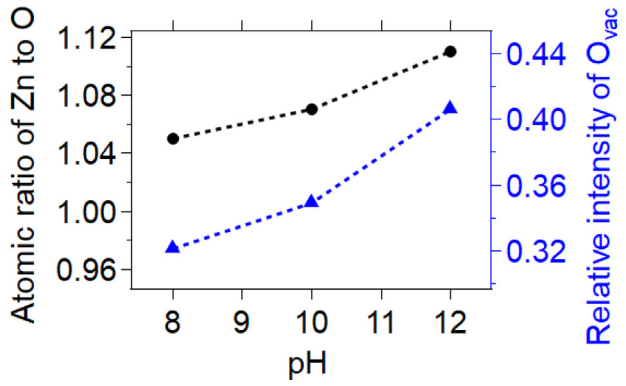

Fig. 7. Atomic ratio of Zn to O and relative intensity of O_{vac} analysed from XPS spectra for all ZnO nanoparticles synthesised at different pHs.

3.6. Electrocatalytic performance of ZnO for hydrogen evolution reaction

The linear polarisation curves of the current density (J) *vs.* the bias potential (E) obtained from the first linear sweep voltammetr (LSV) scan for all ZnO morphologies are presented in Fig. 9(a). The bias potential E was corrected from the 3 M KCl(aq), to the reversible hydrogen electrode (RHE) electrode [69]. On all catalyst modified electrodes, a significant improvement in electrocatalytic activity was observed (i.e. an improvement of ca. 380 mV at J = -30 A m^{-2}) in comparison to the control (unloaded carbon). A current value of 850 μA corresponding to a current density, J, of -30 A m^{-2} was attained at potentials of 2.23 V for the control, 1.88 V for the nanowires, 1.87 V for the nanocuboids, and 1.81 V for the nanospheres (Fig. 9a and Table 2). The position of the potential at which a fixed current density of -30 A m^{-2} is attained, $E_{(J=-30\ \mathrm{A\ m^{-2}})}$ is a reasonable measure of electrocatalytic performance. Specifically for HER, the smaller the magnitude of $E_{(J=-30\ \mathrm{A\ m^{-2}})}$, the lower the energy needed to evolve hydrogen at the same rate, resulting in a higher electrocatalytic performance. Overall, the ZnO nanospheres exhibited the best electrocatalytic performance for the first cycle. The trend in $E_{(J=-30\ \mathrm{A\ m^{-2}})}$ correlates well with the presence of oxygen vacancies (Fig. 7), where the higher the relative intensity of oxygen vacancies, the lower the $E_{(J=-30\ \mathrm{A\ m^{-2}})}$. The value of $E_{(J=-30\ \mathrm{A\ m^{-2}})}$ in our study could not be inversely correlated to the specific surface area (S) of the ZnO nanoparticles as normally expected, since all nanoparticles exhibited relatively similar specific surface areas (Table 1). The perturbation observed in the LSV (especially for the nanospheres) is believed to be due to hydrogen bubbles continuously generated during the measurements, which intermittently blocked the electrode surface. Faster stirring rates for removing the generated bubbles could not be employed as it created a vortex in the solution.

Fig. 9(b) shows the stability of the potential $E_{(J=-30\ \mathrm{A\ m^{-2}})}$ for each catalytic system over a total of 160 scans. Even though the nanospheres gave the best electrocatalytic performance for HER on the first cycle, the HER performance degraded with consecutive scans, with the nanocuboids showing a similar trend. For the control and nanowires, the electrocatalytic performance remained relatively stable with consecutive HER cycles. The aggressive bubble formation during the HER measurements gradually damaged the structure of the ink across the modified electrode's surface, by partially exposing the surface of the GC electrode.

Overall, the electrocatalytic performance and the stability of the catalyst loaded electrode systems are dependent upon a multitude of factors, including: (i) The number of oxygen vacancies on the

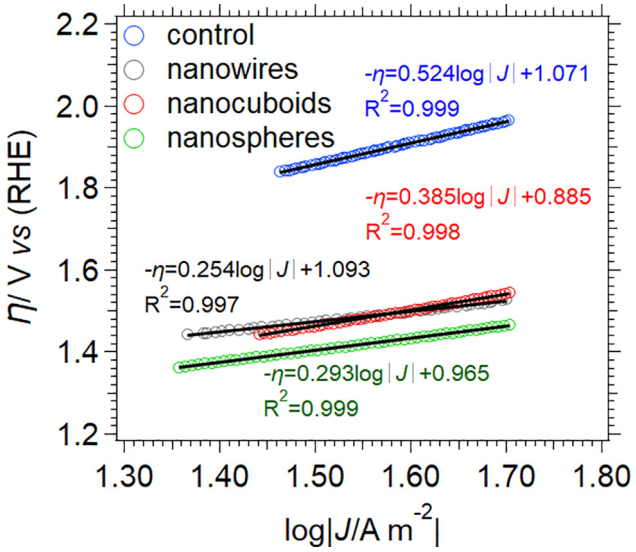

Fig. 8. (a) unit cell structure of w-ZnO along with partial charge on the atoms, (b) top view of 3 × 3 × 2 w-ZnO super cell with oxygen vacancies on (0001) surface, (c) density of states for bulk w-ZnO and 3 × 3 × 2 w-ZnO super-cell with oxygen vacancies on (0001) surface. Black and red lines denote two different spins of electron.

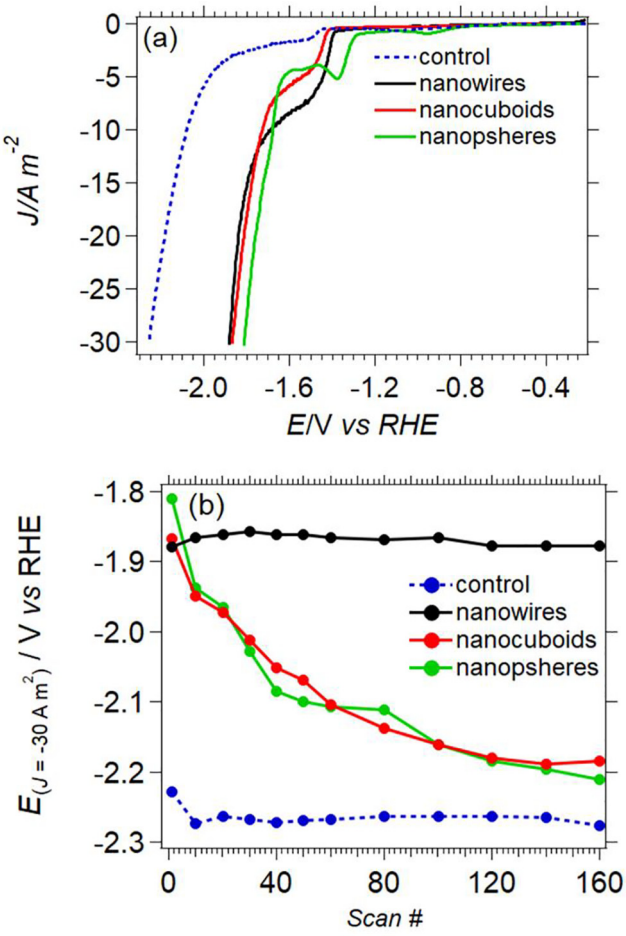

Fig. 9. (a) current density (J) *vs* bias potential (E) linear polarisation curves obtained from the very first hydrogen evolution linear sweep voltammetry (LSV) scan, (b) potentials at $-$ 30 A m^{-2} ($E_{(J=-30\ \mathrm{A\ m^{-2}})}$) *vs* consecutive LSV scan number (*Scan #*) carried out under the same conditions showing the stability of the response with increasing scans.

Table 2
The negative log of exchange current densities ($-\log|J_0|$), Tafel Slope, and the derived charge transfer coefficient, α, analysed from the Tafel plots presented in Fig. 10.

Sample	$-\log\|J_0$ / A cm$^{-2}\|$	Tafel Slope/mV dec^{-1}	α
control	2.04	524	0.11
nanowires	4.30	254	0.23
nanocuboids	2.30	385	0.15
nanospheres	3.29	293	0.20

catalyst surface, (ii) the specific surface area of the catalyst, (iii) the aspect ratios of the catalysts loaded on the electrode, and (iv) the interaction of the catalyst with the ink. In order to achieve the optimal electrocatalytic performance and stability, these factors need to be systematically investigated. This however is beyond the scope of this study; but we plan to perform this investigation in a future work.

Tafel plots of the three electrodes loaded with ZnO nanoparticles with diverse morphologies are presented in Fig. 10, and were derived from the linear polarisation curves in Fig. 9(a). The overpotential (η) is derived by first correcting the potentials (*vs.* 3 M KCl (aq) used) to the reversible hydrogen electrode (RHE) [69], and are calculated using the Nernst equation:

$$\eta = E - E_{eq} = E - \frac{RT}{F}\ln(aH^+)\,, \tag{4}$$

where $-\ln(aH^+)$ is essentially the pH, which is equal to 7 for this work, and all potentials are relative to the RHE.

From the linear fit of the Tafel plots, the negative log of the exchange current densities, the Tafel slope, and the charge transfer coefficient (α) derived from the Tafel Slope [70] are summarised in Table 2. The exchange current density (J_0) represents the baseline current in the absence of net electrolysis (i.e. at zero overpotential) and follows the trend: nanowires $\ll$ nanospheres < nanocuboids < control. The Tafel slope is the amount of change in overpotential ($\Delta\eta$) required to increase the HER current by an order of magnitude. The smaller this value, the better the kinetics of HER are on the given modified electrode. The Tafel slope followed the trend: nanowires < nanospheres < nanocuboids $\ll$ control, suggesting that all ZnO loaded electrodes exhibited greater HER kinetics compared to the control, with the nanowires giving the highest HER kinetics at 254 mV dec^{-1}. The value of α signifies the fraction of overpotential that influences the current density, and follows the inverse trend of the Tafel slopes [71] summarised in Table 2.

4. Conclusions

A simple and cost-effective method for tailoring the morphology of ZnO nanoparticles was proposed where no expensive instrumentation or chemical precursors were required. ZnO nanoparticles, with three different morphologies, were synthesised by applying a sol–gel method at room temperature. It was demonstrated that sodium hydroxide is an effective shape controlling agent for obtaining various morphologies of ZnO nanoparticles and also for manipulating the number of oxygen vacancies in the nanoparticles. All three ZnO morphologies produced higher electrocatalytic activities (i.e. smaller magnitude of potential required to maintain hydrogen evolution at -30 A m^{-2}) and kinetics (lower Tafel slope) towards the splitting of water (at pH = 7.0) compared to the unloaded carbon control. This study is of great importance both fundamentally and practically since it introduces a new simple and cost-effective method for developing nanocatalysts and testing them as cathode materials for water splitting devices for the production of hydrogen.

Declaration of Competing Interest

The authors declare that they have no known competing financial interests or personal relationships that could have appeared to influence the work reported in this paper.

Acknowledgments

MVS acknowledges the financial support from the Research and Development Committee Small Grant Program 2018 from Curtin University, and of the UCD Ad Astra fellowship programme. MP and DSS acknowledges the financial support of an Australian Research Council (ARC) Future Fellowship (FT160100303, FT170100315). CEB acknowledges the financial support of the

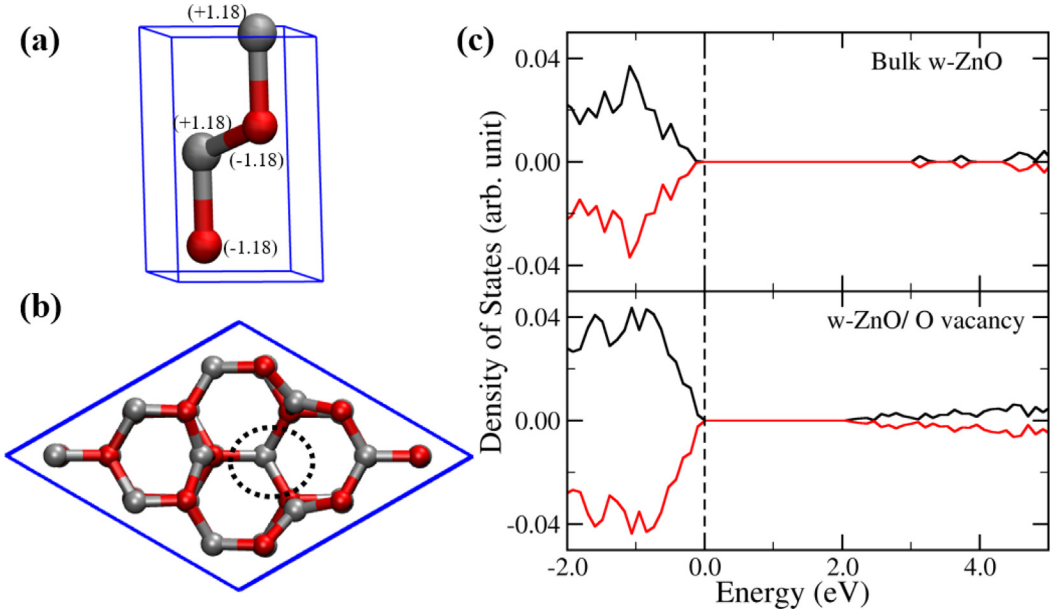

Fig. 10. Tafel plots of the nanowires, nanocuboids, nanospheres loaded in ink, as well as the unloaded ink control, derived from the linear polarisation curves in Fig. 9(a). The linear regression of the plots is represented by the darker dashed lines of the same colour, and the equations of the linear fits are also shown.

ARC for LIEF grants LE0775551, LE120100026 and LE140100075, which enabled the XRD, XPS and SAXS measurements to be undertaken. PKS and NJE acknowledge Science Foundation Ireland (SFI) grant 17/NSFC/5229 and Enterprise Ireland grant CF2017077 for research funding. The authors acknowledge the facilities and technical assistance of the Microscopy & Microanalysis Facility of the John de Laeter Centre at Curtin University. Small angle X-ray scattering (SAXS) data was also collected on the SAXS beamline at the Australian Synchrotron, part of ANSTO.

Appendix A. Supplementary data

Supplementary data to this article can be found online at https://doi.org/10.1016/j.jechem.2020.07.051.

References

[1] J. Masa, P. Weide, D. Peeters, I. Sinev, W. Xia, Z. Sun, C. Somsen, M. Muhler, W. Schuhmann, Adv. Energy Mater. 6 (2016) 1502313.
[2] J. Greeley, T.F. Jaramillo, J. Bonde, I.B. Chorkendorff, J.K. Norskov, Nat Mater. 5 (2006) 909–913.
[3] H.A. Gasteiger, N.M. Markovic, Science 324 (2009) 48–49.
[4] Y. Zheng, Y. Jiao, M. Jaroniec, S.Z. Qiao, Angew. Chem. 54 (2015) 52–65.
[5] J.M. Ogden, Annu. Rev. Environ. Resour. 24 (1999) 227–279.
[6] C. Wang, Y. Gao, L. Wang, P. Li, Phys. Status Solidi A 214 (2017) 1600876.
[7] M.R. Alenezi, A.S. Alshammari, K.D. Jayawardena, M.J. Beliatis, S.J. Henley, S.R. Silva, J. Phys. Chem. C 117 (2013) 17850–17858.
[8] M.R. Hasan, S.H. Baek, K.S. Seong, J.H. Kim, I.K. Park, ACS Appl. Mater. Interfaces 7 (2015) 5768–5774.
[9] S.H. Ko, D. Lee, H.W. Kang, K.H. Nam, J.Y. Yeo, S.J. Hong, C.P. Grigoropoulos, H.J. Sung, Nano Lett. 11 (2011) 666–671.
[10] Q. Wan, Q.H. Li, Y.J. Chen, T.H. Wang, X.L. He, J.P. Li, C.L. Lin, Appl. Phys. Lett. 84 (2004) 3654–3656.
[11] S.Z. Mousavisani, J.B. Raoof, K.Y. Cheung, A.R.H. Camargo, T. Ruzgas, A.P.F. Turner, W.C. Mak, Biosens. Bioelectron. 128 (2019) 159–165.
[12] S. Wirunchit, C. Apivitcholchat, T. Chodjarusawad, W. Koetniyom, AIP Conf. Proc. 2010 (2018) 020024.
[13] H.J. Seok, A. Ali, J.H. Seo, H.H. Lee, N.E. Jung, Y. Yi, H.K. Kim, Sci. Technol. Adv. Mater. 20 (2019) 389–400.
[14] S.P. Gupta, A.S. Pawbake, B.R. Sathe, D.J. Late, P.S. Walke, Sensors Actuat. B-Chem. 293 (2019) 83–92.
[15] K. Noh, M. Kim, S.-H. Lee, H.-S. Yun, T.-H. Lim, Y. Choi, K.-J. Kim, Y. Jiang, K. Beom, M. Kim, Y.-G. Kim, P. Lee, N. Oh, B.H. Kim, C. Shin, H.H. Lee, T.-S. Yoon, M. Shim, J. Lim, K.-B. Kim, S.-Y. Cho, Curr. Appl. Phys. 19 (2019) 998–1005.
[16] X. Yang, P.N. Ni, P.T. Jing, L.G. Zhang, R.M. Ma, C.X. Shan, D.Z. Shen, P. Genevet, Adv. Opt. Mater. 7 (2019) 1801681.
[17] R. Gao, X. Cheng, S. Gao, X. Zhang, Y. Xu, H. Zhao, L. Huo, Appl. Surf. Sci. 485 (2019) 266–273.
[18] S. Meephon, T. Rungrotmongkol, S. Puttamat, S. Praserthdam, V. Pavarajarn, J. Environ. Sci. 84 (2019) 97–111.
[19] S. Payra, S. Challagulla, Y. Bobde, C. Chakraborty, B. Ghosh, S. Roy, J. Hazard. Mater. 373 (2019) 377–388.
[20] J.G. Clar, W.E. Platten 3rd, E. Baumann, A. Remsen, S.M. Harmon, K. Rodgers, T. A. Thomas, J. Matheson, T.P. Luxton, Sci. Total Environ. 670 (2019) 78–86.
[21] H. Mohammadi, A. Kamkar, A. Misaghi, M. Zunabovic-Pichler, S. Fatehi, Food Packaging Shelf 21 (2019) 100330.
[22] B. Manikandan, T. Endo, S. Kaneko, K.R. Murali, R. John, J. Mater. Sci. Mater. Electron. 29 (2018) 9474–9485.
[23] J. Ungula, B.F. Dejene, Physica B Condensed Matter. 480 (2016) 26–30.
[24] H. Ghorbani, F. Mehr, H. Pazoki, B. Rahmani, Orient J. Chem. 31 (2015) 1219–1221.
[25] S.S. Kumar, P. Venkateswarlu, V.R. Rao, G.N. Rao, Int. Nano Lett. 3 (2013).
[26] C. Rodwihok, S. Choopun, P. Ruankham, A. Gardchareon, S. Phadungdhitidhada, D. Wongratanaphisan, Appl. Surf. Sci. 477 (2019) 159–165.
[27] Y. Han, C.-B. Yao, Y.-T. Cao, S.-Q. Li, Opt Laser Technol. 108 (2018) 619–625.
[28] S. Kaassamani, W. Kassem, M. Tabbal, Appl. Surf. Sci. 473 (2019) 298–302.
[29] S. Agarwal, P. Rai, E.N. Gatell, E. Llobet, F. Güell, M. Kumar, K. Awasthi, Sensor Actuat. B-Chem. 292 (2019) 24–31.
[30] L. Huang, Z. Yang, Y. Shen, P. Wang, B. Song, Y. He, W. Yang, H. Wang, Z. Wang, Y. Chen, Mater. Chem. Phys. 232 (2019) 129–136.
[31] S. Delice, M. Isik, N.M. Gasanly, Mater. Lett. 245 (2019) 103–105.
[32] A. Sangeetha, S. Jaya Seeli, K.P. Bhuvana, M.A. Kader, S.K. Nayak, J. Sol-Gel Sci. Technol. 91 (2019) 261–272.
[33] M.A. Boda, B. Bozkurt Çırak, Z. Demir, Ç. Çırak, Mater. Lett. 248 (2019) 143–145.
[34] F. Qiao, Q. Liang, J. Yang, Z. Chen, Q. Xu, J. Electron. Mater. 48 (2019) 2338–2342.
[35] N. Pauzi, N. Mat Zain, N.A. Ahmad Yusof, Bull. Chem. React. Eng. Catal. 14 (2019) 182.
[36] B. Nageswara Rao, E.S. Srinadhu, V. Madhusudhanrao, N.T. Satyanarayana, Indian Ceram. Soc. 77 (2018) 169–174.
[37] L.K. Babu, E. Sarala, O. Audiseshaiah, K.M. Reddy, Y.V.R. Reddy, Surf. Interface 16 (2019) 93–100.
[38] S. Das, K. Dutta, A. Pramanik, CrystEngComm 15 (2013) 6349.
[39] S. Cho, J.W. Jang, S.H. Jung, B.R. Lee, E. Oh, K.H. Lee, Langmuir 25 (2009) 3825–3831.
[40] H. Lu, S. Wang, L. Zhao, J. Li, B. Dong, Z. Xu, J. Mater. Chem. 21 (2011) 4228.
[41] D. Patil, V. Deo, S. Bagul, P. Patil, P. Sonawane, M. Wagh, J. Nanostruct. 8 (2018) 11–20.
[42] P. Hu, X. Zhang, N. Han, W. Xiang, Y. Cao, F. Yuan, Cryst. Growth Des. 11 (2011) 1520–1526.
[43] L. Song, S. Zhang, X. Wu, Q. Wei, Ind. Eng. Chem. Res. 51 (2012) 4922–4926.
[44] M. Navaneethan, J. Archana, Y. Hayakawa, CrystEngComm 15 (2013) 8246.
[45] J.A. Potton, G.J. Daniell, B.D. Rainford, J. Appl. Crystallogr. 21 (1988) 663–668.
[46] J.A. Potton, G.J. Daniell, B.D. Rainford, J. Appl. Crystallogr. 21 (1988) 891–897.
[47] P.R. Jemian, J.R. Weertman, G.G. Long, R.D. Spal, Acta Mater. 39 (1991) 2477–2487.
[48] O. Spalla, S. Lyonnard, F. Testard, J. Appl. Crystallogr. 36 (2003) 338–347.
[49] G. Beaucage, J. Appl. Crystallogr. 28 (1995) 717–728.
[50] J. Ilavsky, P.R. Jemian, J. Appl. Crystallogr. 42 (2009) 347–353.
[51] G. BeaucageJ, Appl. Crystallogr. 29 (1996) 134–146.
[52] A.J. Hurd, D.W. Schaefer, D.M. Smith, S.B. Ross, A. Le Méhauté, S. Spooner, Phys. Rev. B 39 (1989) 9742–9745.
[53] J.P. Perdew, K. Burke, M. Ernzerhof, Phys. Rev. Lett. 77 (1996) 3865–3868.
[54] G. Kresse, J. Furthmüller, Phys. Rev. B 54 (1996) 11169.
[55] G. Kresse, J. Furthmüller, Comput. Mat. Sci. 6 (1996) 15–50.
[56] G. Kresse, J. Hafner, Phys. Rev. B 47 (1993) 558.
[57] G. Kresse, J. Hafner, Phys. Rev. B 49 (1994) 14251.
[58] X. Ma, Y. Wu, Y. Lv, Y. Zhu, J. Phys. Chem. C 49 (2013) 26029–26039.
[59] C.-F. Liu, Y.-J. Lu, C.-C. Hu, ACS Omega 3 (2018) 3429–3439.
[60] S.I.M. Zayed, H.A.M. Arida, Int. J. Electrochem. Sci. 8 (2013) 1340–1348.
[61] M. Elkady, H. Hassan, Curr. Nanosci. 11 (2015) 805–814.
[62] H. Shokry Hassan, A.B. Kashyout, I. Morsi, A.A.A. Nasser, A. Raafat, Sens Biosensing Res. 1 (2014) 34-40.
[63] Z. Gaburro, P.M. Aneesh, S. Cabrini, K.A. Vanaja, M.K. Jayaraj, Nanophotonic Mater. IV 6639 (2007) 66390J.
[64] X. Ma, H. Zhang, Y. Ji, J. Xu, D. Yang, Mater. Lett. 59 (2005) 3393–3397.
[65] Q. Zhao, L. Fu, D. Jiang, J. Ouyang, Y. Hu, H. Yang, Y. Xi, Commun. Chem. 2 (2019) 11.
[66] L. Wang, Y. Yu, H. He, Y. Zhang, X. Qin, B. Wang, Sci. Rep. 7 (2017) 12845.
[67] P.T. Hsieh, Y.C. Chen, K.S. Kao, C.M. Wang, Appl. Phys. A 90 (2008) 317–321.
[68] F. Oba, A. Togo, I. Tanaka, J. Paier, G. Kresse, Phys. Rev. B 77 (2008).
[69] D.K. Nordstrom, F.D. Wilde, Reduction-oxidation Potential (Electrode Method), U.S. Geological Survey, Reston VA, 2005, pp. 4–19.
[70] K.T. Lee, H.S. Yoon, J.S. Ahn, E.D. Wachsman, J. Mater. Chem. 22 (2012) 17113–17120.
[71] A.J. Bard, L.R. Faulkner, Electrochemical Methods. Fundamentals and Applications, second ed., Wiley, New York, 2001.